

Entropy production in the nonreciprocal Cahn-Hilliard modelThomas Suchanek,¹ Klaus Kroy,¹ and Sarah A. M. Loos^{2,*}¹*Institut für Theoretische Physik, Universität Leipzig, Postfach 100 920, D-04009 Leipzig, Germany*²*DAMTP, Centre for Mathematical Sciences, University of Cambridge, Wilberforce Road, Cambridge CB3 0WA, United Kingdom*

(Received 11 May 2023; accepted 13 November 2023; published 18 December 2023)

We study the nonreciprocal Cahn-Hilliard model with thermal noise as a prototypical example of a generic class of non-Hermitian stochastic field theories, analyzed in two companion papers [Suchanek, Kroy, and Loos, *Phys. Rev. Lett.* **131**, 258302 (2023); *Phys. Rev. E* **108**, 064123 (2023)]. Due to the nonreciprocal coupling between two field components, the model is inherently out of equilibrium and can be regarded as an active field theory. Beyond the conventional homogeneous and static-demixed phases, it exhibits a traveling-wave phase, which can be entered via either an oscillatory instability or a critical exceptional point. By means of a Fourier decomposition of the entropy production rate, we quantify the associated scale-resolved time-reversal symmetry breaking, in all phases and across the transitions, in the low-noise regime. Our perturbative calculation reveals its dependence on the strength of the nonreciprocal coupling. Surging entropy production near the static-dynamic transitions can be attributed to entropy-generating fluctuations in the longest wavelength Fourier mode and heralds the emerging traveling wave. Its translational dynamics can be mapped on the dissipative ballistic motion of an active (quasi)particle.

DOI: [10.1103/PhysRevE.108.064610](https://doi.org/10.1103/PhysRevE.108.064610)**I. INTRODUCTION**

A predator chasing fleeing prey [1] or the vision-cones restricting interactions [2–4] between herding animals are vivid examples of nonreciprocal interactions, ubiquitous in nonequilibrium many-body systems. Likewise, the effective interactions between colloids in flows [5], active particles [6,7], or in mixtures of active and passive particles [8–10] break the action-reaction principle on the microscale. Nonreciprocal couplings between different order parameter fields (such as density and polarization fields) also commonly occur in active field theories [11–14]. More generally, recent research has made clear that the concept of nonreciprocal dynamics provides a unifying perspective on a wide range of nonequilibrium phenomena, including waves on membranes [12], oscillatory patterns in (binary) fluids [10,14–16], or odd elasticity in soft crystals [17,18]. In field-theoretical models, nonreciprocal coupling between field components may entail the occurrence of parity-time (\mathcal{PT})-symmetry breaking transitions where dissipative order-parameter patterns emerge, most commonly via oscillatory instabilities (or Hopf-bifurcations) [19,20] and the recently uncovered critical exceptional points (CEPs) [13,21,22], all of which can be understood from the viewpoint of non-Hermitian dynamics [13,23]. From the perspective of bifurcation theory [24,25],

both transition scenarios are linear instabilities of the dynamics and can be characterized by the linearized dynamical operator’s eigenvalues and eigenmodes that become unstable in the course of the transition. For oscillatory instabilities, the eigenvalue of the critical mode is complex and becomes purely imaginary at the transition. At CEPs, a vanishing real eigenvalue is accompanied by the coalescence of unstable eigenmodes.

The nonreciprocal Cahn-Hilliard model has been recognized as prototypical in this respect [26–28]. It exhibits a traveling-wave phase with two associated \mathcal{PT} -symmetry breaking transitions [see Fig. 1(d)], one via a line of critical exceptional points; yet it is simple enough to be studied analytically. The traveling wave phase is a paradigmatic example of how dynamical phases of traveling patterns in non-Hermitian field models are always characterized by a coupling of the broken parity of a spatial pattern and the sense of motion, and thus by \mathcal{PT} symmetry breaking. The Cahn-Hilliard model consists of two field components, each evolving according to a gradient dynamics, which can be thought of as the densities of two (de)mixing substances. In the nonreciprocal version, the interaction between the components is not mutually symmetric, and therefore violates the reciprocity principle that is a cornerstone of any equilibrium system. The dynamics of such a nonreciprocal field model can therefore not be understood from the perspective of one global effective potential (or “nonequilibrium free energy”), but rather as a “dynamical frustration”: while field A tries to relax to a more favorable state, it pushes field B into a state of higher local energy; and vice versa [29]. By analogy with two particles obeying a run-and-catch relation, this also illustrates the basic mechanism that causes the emergence of traveling patterns. On the level of eigenmode dynamics, a traveling

*sl2127@cam.ac.uk

Published by the American Physical Society under the terms of the [Creative Commons Attribution 4.0 International](https://creativecommons.org/licenses/by/4.0/) license. Further distribution of this work must maintain attribution to the author(s) and the published article’s title, journal citation, and DOI.

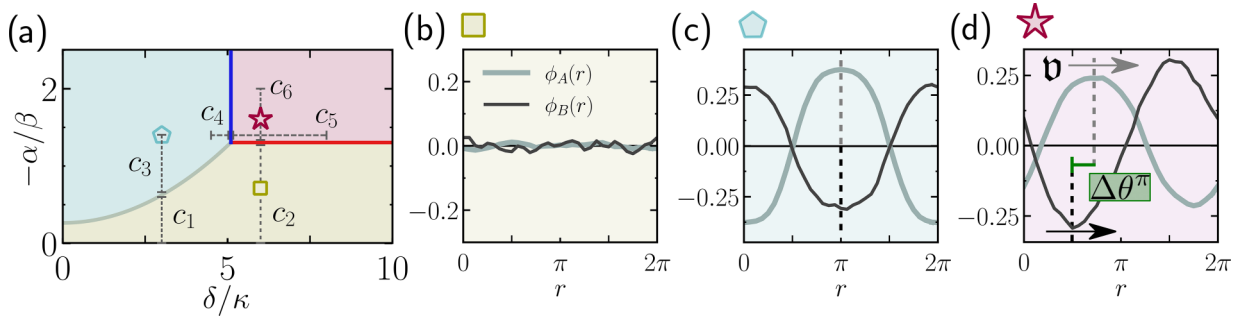


FIG. 1. (a) Phase diagram of the stationary solutions of Eq. (1) as established in Ref. [26] for $\kappa = 0.01$, $\gamma = 0.015$ and $\beta = 0.05$. The mixed phase is marked in yellow, the static-demixed phase in blue and the traveling-wave phase in red. The transition from the static-demixed phase to the traveling wave phase is through a line of exceptional points, which is here marked by a vertical blue line. The transition from the homogeneous phase to the traveling wave phase is through a line of oscillatory instabilities, here marked by a horizontal red line. The dotted gray lines (c_1 – c_6) mark paths along which the behavior of the entropy production is displayed in Figs. 2, 4, and 5; (b)–(d) snapshots of the stationary solutions for $\epsilon = 2.5 \times 10^{-5}$. Unlike to the static-demixed phase, the maxima and minima of the profiles of the fields ϕ_A (gray) and ϕ_B (black) in the traveling-wave phase have a characteristic mean phase shift $\langle \Delta\theta^\pi \rangle > 0$, with $\Delta\theta^\pi \equiv \theta_A - (\theta_B - \pi)$, which is aligned with the direction of propagation. This coupling of the propagation direction to the relative phase shift (which determines the parity of the profile) entails the \mathcal{PT} symmetry breaking in the nonreciprocal Cahn-Hilliard model.

wave can be characterized as a “chase” along the Goldstone mode [13], which itself tends to dynamically restore a spontaneously broken symmetry.

Compared to the phase behavior of nonreciprocal many-body systems, their fluctuations are, so far, much less understood. A particularly intriguing question concerns the time-reversal symmetry breaking (TRSB) of the fluctuations of nonreciprocal systems, which can be quantified by the (“informatic”) entropy production rate \mathcal{S} [30,31]. Indeed, from the analogy with the dynamically frustrated run-and-catch dynamics, we may wonder how the fluctuations reflect the emergence of the collective organization and mesoscale phases. Conversely, since traveling waves break time-reversal symmetry on the mesoscopic and deterministic level, one may wonder whether this is already the case for transient fluctuations.

In two companion papers [32,33] we prove such a statement for a broad class of non-Hermitian models, which includes the nonreciprocal Cahn-Hilliard model studied here. Namely, we show that \mathcal{S} exhibits, quite generally, a characteristic signature at continuous static-dynamic phase transitions. Here, we provide a more explicit and detailed analysis of TRSB for said model, by means of simulations and perturbative analytical calculations. We explicitly consider \mathcal{S} near the two dissimilar types of static-dynamic phase transitions, namely an oscillatory instability and a CEP, in the low-noise regime. To this end, we first introduce a Fourier decomposition of the entropy production rate \mathcal{S} . It enables us to calculate \mathcal{S} numerically for the full parameter range of the phase diagram, and also provides the basis for our perturbative approaches. We find that \mathcal{S} increases steeply toward the static-dynamic transitions, as predicted by our general theory [32,33]. Moreover, our perturbative analytical expressions for the Fourier contributions unravel the scale-dependence of the entropy production, in all phases. This is crucial for a qualitative understanding of how TRSB arises, and with which physical features it is associated. For example, by extracting the precise scaling of \mathcal{S} in the noise intensity, we can determine whether the fluctuations retain their nonequilibrium

character in the deterministic (zero-noise) limit. Furthermore, an important result, which follows from these analytical considerations, is the role of the translational fluctuations of the demixing profiles, in the static-demixed phase. The latter are shown to account for most of the incipient entropy production. Interestingly, as we rigorously show in Ref. [32], the dynamics of the associated patterns can be mapped onto the persistent motion of an active (quasi)particle, illuminating its dissipative character.

The paper is structured as follows. In Sec. II, we introduce the model and framework, and present the spectral decomposition of the entropy production rate. In Sec. III, we derive approximative solutions for \mathcal{S} in the low-noise regime, studying each of the phases and the associated transition scenarios, separately. To tackle \mathcal{S} in the static-demixed phase, we need to develop a refined approach and make some further suitable assumptions. We reinforce our analytical predictions by comparing them with simulation results, throughout. To improve readability, some of the technical aspects are given in the Appendix.

II. FRAMEWORK AND MODEL

A. Noisy nonreciprocal Cahn-Hilliard model

We study a stochastic version of the nonreciprocal Cahn-Hilliard model [26,27,34] of the two-component field $\phi(r, t) = (\phi_A, \phi_B)^T$, where $t \in \mathbb{R}$ denotes the time and r the continuous spatial coordinate. The dynamical equations of the two field components read

$$\begin{aligned}\dot{\phi}_A &= \nabla[(\alpha + \phi_A^2 - \gamma \nabla^2)\nabla\phi_A + (\kappa - \delta)\nabla\phi_B + \sqrt{2\epsilon}\Lambda_A], \\ \dot{\phi}_B &= \nabla[\beta\nabla\phi_B + (\kappa + \delta)\nabla\phi_A + \sqrt{2\epsilon}\Lambda_B],\end{aligned}\quad (1)$$

where we use the compact notation, $\dot{\phi} = \partial_t \phi$. The parameters κ and δ give the strength of the reciprocal (symmetric) and nonreciprocal (asymmetric) coupling, respectively, between the fields. We study the dynamics in one spatial dimension on the domain $r \in [0, L]$ with periodic boundary conditions, and focus on the long-time limit $t \rightarrow \infty$. The noise terms

$\sqrt{2\epsilon}\Lambda$ are zero-mean, unit-variance, Gaussian white-noise fields, constructed such that in the case $\delta = 0$, the resulting statistical field theory obeys a fluctuation–dissipation relation [35], in which ϵ plays the role of temperature. The parameters α and β and γ control the conventional “demixing,” where α and β control the amplitude of the demixed state and γ the interface width. In our numerical examples, we keep $\beta = 0.05$ while varying α . Furthermore, we fix $\kappa = 0.01$, corresponding to a weakly repulsive, reciprocal coupling between the fields, while varying the strength of the nonreciprocal coupling δ .

For some background on the general properties of the model in Eq. (1), including its phase behavior, the morphology of its stationary states, and coarsening dynamics, we refer the Reader to Refs. [26,27,34,36].

1. Phase behavior

The stationary solutions of Eq. (1) in the noise-free limit, which we denote by ϕ^* , can be parametrized as

$$\phi_{A,B}^*(r, t) = \sum_{k>0} \mathcal{A}_{A,B}^{k,*} \cos [q_k r + \theta_{A,B}^{k,*}(t)], \quad (2)$$

by Fourier modes with wave numbers $q_k \equiv 2\pi k/L$ for odd $k \in \{2n+1 : n \in \mathbb{N}_0\}$, amplitudes $\mathcal{A}_{A,B}^{k,*}$ and phases $\theta_{A,B}^{k,*}(t)$. It is known that ϕ^* exhibits three distinct phases as depicted in Fig. 1 [26]: first a homogeneous, or “mixed” phase ($\mathcal{A}_{A,B}^{k,*} = 0$) for positive and small negative α , which gives way to a second, inhomogeneous or “demixed” state upon a decrease of α below α_c . For negative or small positive values of the nonreciprocity δ , the demixed state is static with $\mathcal{A}_{A,B}^{k,*} > 0$, $\theta_{A,B}^{k,*}(t) = \text{const.}$ In contrast, if δ exceeds the critical threshold $\delta_c \equiv \sqrt{\beta^2 + \kappa^2}$, the model admits a third phase with traveling-wave solutions ($\mathcal{A}_{A,B}^{k,*} > 0$, $\dot{\theta}_{A,B}^{k,*}/q_1 = \mathbf{v}$). Its propagation velocity is $\mathbf{v} = \pm \sqrt{\delta^2 - \delta_c^2}$, and its direction is randomly set by the noise and initial condition [26], such that, for an ensemble with random initial conditions and noise, $\langle \dot{\theta}_{A,B}^{k,*} \rangle = 0$, with $\langle \cdot \rangle$ denoting the noise average. The direction of the wave propagation is (on average) aligned with a characteristic phase shift $\Delta\theta^{*,\pi} = \theta_A^* - (\theta_B^* - \pi)$, i.e., with the parity of the wave profiles [26,32], see Fig. 1(d) for an illustration. In each parameter region of the phase diagram [Fig. 1(a)], only a single stationary solution ϕ^* is linearly stable, so that after a phase boundary is crossed, a spontaneous transition to the new stable phase occurs.

The transition from the homogeneous to the traveling-wave state, e.g., observable along the path c_2 , occurs through an oscillatory instability [solid horizontal red line in Fig. 1(a)]. The transition from the static-demixed state to the traveling-wave state, e.g., observable on the path c_4 , is via a line of critical exceptional points [37] [solid vertical blue line in Fig. 1(a)]. For an in-depth description of the characteristics of critical exceptional points, in this context, we refer to Refs. [13,33]. Furthermore, it has been shown that in a fairly large region of the phase diagram above the demixing transitions, the first Fourier mode is dominant in the two demixed states [26], i.e., $\mathcal{A}^{1,*} \gg \mathcal{A}^{k,*}$ for all $k > 1$.

Our numerical investigations of Eq. (1) reveal that in the regime of small $\epsilon > 0$ the phase diagram in Fig. 1 remains essentially unchanged compared to the zero-noise case. Yet the transition points widen into an extended region (details about

the numerics are given in Sec. IID and Appendix B). Nevertheless, it is important to take noise into account, because even a small intensity noise brings to light strong fluctuations, which appear exclusively in the vicinity of the phase transitions—in analogy to equilibrium critical phenomena. However, in sharp contrast to equilibrium critical phenomena, here these strong fluctuations possess strong time-reversal asymmetry, leading to new phenomena such as (long-lived) transient traveling waves and actively enhanced interfacial dynamics, which substantially alter the appearance of the stationary state, as we demonstrate in Ref. [32]. In this article, we investigate the entropy production associated with these new noise-induced phenomena in more detail.

2. Nonequilibrium currents and model structure

The dynamical equations (1) can be recast into the following form to better reveal their general structure:

$$\dot{\phi}_{A,B} = -\nabla \cdot (J_{A,B}^d + \sqrt{2\epsilon}\Lambda_{A,B}), \quad (3)$$

$$J_{A,B}^d = -\nabla \left(\frac{\delta \mathcal{F}}{\delta \phi_{A,B}} + \mu_{A,B}^a \right). \quad (4)$$

The deterministic current in Eq. (4) is composed of two parts. Its equilibrium-like contribution derives from a scalar potential

$$\mathcal{F} = \int_V dr \frac{1}{2} \left[\alpha \phi_A^2 + \frac{1}{6} \phi_A^4 + \beta \phi_B^2 + \gamma (\nabla \phi_A)^2 \right], \quad (5)$$

corresponding to the free energy of a standard Cahn-Hilliard field ϕ_A coupled to a Gaussian field ϕ_B . Its nonequilibrium component is generated by a nonequilibrium chemical potential

$$\mu^a = \delta (-\phi_B, \phi_A)^T. \quad (6)$$

Since it cannot be represented as variation of a scalar potential, μ^a is a source of currents that are not compatible with thermal equilibrium. This decomposition unveils that the nonreciprocity of the coupling between ϕ_A and ϕ_B implies by itself a deviation from equilibrium-like dynamics. Note that other decompositions can be chosen, but the one in Eqs. (3) and (4) clearly separates equilibrium-compatible and inherently nonequilibrium dynamics [38].

B. Measuring irreversibility

A suitable measure of the nonequilibrium character of mesoscopic models is provided by the TRSB of their fluctuations [30,31,39]. We quantify the latter for Eq. (1), using the (informatic) entropy production rate for field models and the techniques developed in Refs. [30,31,33]. In this context, the entropy production along a given trajectory $\{\phi_{t \in [0, T]}\}$ is defined as the log ratio of the path probabilities [40] for the observation of that trajectory and its time-reversed realization $\{\phi_{t \in [0, T]}^R\}$,

$$s[\phi; 0, T] \equiv \log \frac{\mathbb{P}[\{\phi_{t \in [0, T]}\}]}{\mathbb{P}[\{\phi_{t \in [0, T]}^R\}]} \quad (7)$$

The fields are assumed to be position-like and thus even under time reversal. The average entropy production rate

$$\mathcal{S} = \lim_{dt \rightarrow 0} \langle s[\phi; t, t + dt]/dt \rangle, \quad (8)$$

with the time increment $dt \in \mathbb{R}_+$, serves as a measure of the average TRSB at time t . By construction, \mathcal{S} is constant in time for any steady state. In particular, $\mathcal{S} = 0$ in thermal equilibrium, where $\mu^a = 0$.

In the vicinity of the phase transitions, the zero-noise limit

$$\mathcal{S}^* = \lim_{\epsilon \rightarrow 0} \mathcal{S} \quad (9)$$

is particularly interesting [32]. While not a natural observable itself, \mathcal{S}^* is a means to extract quantitative information about the TRSB at leading order in ϵ . In Refs. [32,33], we have shown that for models of the type of Eq. (3), \mathcal{S}^* exhibits a characteristic behavior across continuous phase transitions from a static to a dynamical phase. Specifically, both for oscillatory instabilities and CEPs, we have demonstrated that \mathcal{S} generally surges toward the transition point and scales like the susceptibility. In the following, we present a detailed analytical and numerical investigation of this phenomenon for the concrete model of Eq. (1), in the low-noise limit.

C. Decomposition of \mathcal{S}

We first derive a decomposition of \mathcal{S} in terms of contributions from different Fourier modes, which forms the basis for our analytical and numerical investigations, and provides insights into TRSB at different scales.

We start from the general expression for models of the type of Eq. (3),

$$\mathcal{S} = \int_V dr \frac{\sum_i \langle J_i^d \nabla \mu_i^a \rangle}{\epsilon} - \int_V dr \sum_i \left\langle \frac{\delta}{\delta \phi_i} \nabla^2 \mu_i^a \right\rangle, \quad (10)$$

which we derived in Ref. [33]. Exploiting that the nonequilibrium chemical potential given in Eq. (6) is totally antisymmetric in the field components, Eq. (10) simplifies to

$$\mathcal{S} = \int_0^L dr \frac{\delta}{\epsilon} \left[\langle J_A^d(r) \nabla \phi_B(r) \rangle - \langle J_B^d(r) \nabla \phi_A(r) \rangle \right]. \quad (11)$$

Further, using that, in the stationary state,

$$0 = \int_0^L dr \partial_t \langle \phi_A \phi_B \rangle = \int_0^L dr \left(\langle J_A^d \nabla \phi_B \rangle + \langle J_B^d \nabla \phi_A \rangle \right),$$

we find

$$\mathcal{S} = -\epsilon^{-1} 2\delta \int_0^L dr \langle J_B^d \nabla \phi_A \rangle. \quad (12)$$

Now we transform the last expression to Fourier space, according to

$$\phi_{A,B}^k \equiv L^{-1} \int_0^L dr \phi_{A,B}(r) e^{-iq_k r}. \quad (13)$$

Plugging in the explicit expression Eq. (4) for J_B^d , we find the linear decomposition

$$\mathcal{S} = \sum_{k=1}^{\infty} \sigma^k, \quad (14)$$

with Fourier components

$$\sigma^k = \frac{\delta 4Lq_k^2}{\epsilon} \left[\beta \text{Re} \langle \phi_A^k \phi_B^{-k} \rangle + (\kappa + \delta) \langle |\phi_A^k|^2 \rangle \right]. \quad (15)$$

Importantly, although the nominal Fourier mode contribution σ^k to the entropy production rate depends only on the statistics of ϕ^k , it cannot strictly be assigned exclusively to the dynamics of ϕ^k . Recalling the definition of \mathcal{S} in terms of the path probabilities of the full process ϕ , such an assignment would only be legitimate if the dynamics of the k th Fourier mode was statistically independent of all other modes. Indeed, in this case, the entropy production rate of the k th mode would be a well-defined quantity, and equal to σ^k as given in Eq. (15). For our model, this is never strictly the case. However, such stochastic independence indeed approximately holds under certain conditions, which we discuss in detail in Sec. III.

In any case, Eq. (15) provides a representation of \mathcal{S} exclusively in terms of quadratically expectation values of $\phi_{A,B}$. The latter can be calculated perturbatively up to linear order in ϵ to make further analytical progress (see Sec. III) and to determine \mathcal{S}^* exactly. As a bonus, the representation given in Eq. (15) is also convenient for numerical calculations of \mathcal{S} throughout the phase diagram (see Appendix D).

D. Numerical method and UV cutoff

To numerically integrate Eq. (1) for small values of ϵ we used a Euler-Maruyama algorithm with finite difference gradients on a domain of length $L = 2\pi$, discretized by 32 equally spaced mesh points, and time slices $\Delta t = 0.01$. We determine the numerical value of $\phi_{A,B}^k$ as well as the statistics of $\phi_{A,B}^k$. For the mixed phase, we use the latter to numerically evaluate the Fourier mode contributions σ^k as defined in Eq. (15). For the demixed phases, we use an alternative route to calculate \mathcal{S} based on the decomposition of phase and amplitude [as in Eq. (2)] described in Appendix B. It offers the possibility to separately calculate the contribution due to the fluctuations that lead to displacements of the interfaces between ϕ_A and ϕ_B , which are of special interest [32]. It also turned out to provide a much faster numerical convergence.

A general observation from the numerical data is that, in the steady state and low-noise regime, only the lowest Fourier modes are coupled, in all three phases. Furthermore, consistent with our analytical results presented below in Eq. (20) and Appendix D, σ^k quickly converges to a function that depends on δ and γ only, in all phases. The underlying mathematical reason is that for higher k , the highest-order differential operator ∇^3 in Eq. (1) completely dominates J^d (see Appendix D). This also implies that \mathcal{S} is always formally divergent, as a consequence of the usual ‘‘UV catastrophe,’’ which is cured by introducing a cutoff length scale [the cutoff length scale can be thought of as the maximum resolution with which the process defined in Eq. (1) is observed, or a microscale beyond which the continuous field description breaks down]. Our numerical computations showed that, for the parameter regime we investigated, the choice $k = 5$ is appropriate to study the change of the behavior of \mathcal{S} . Further details are provided in Appendix B. Moreover, in Appendix E, we discuss possibilities to introduce a cutoff length without spoiling the

genuinely probabilistic interpretation of \mathcal{S} in terms of path probabilities.

III. IRREVERSIBILITY IN THE DIFFERENT PHASES AND ACROSS THE TRANSITIONS

Equipped with the framework described in Sec. II, we now analytically and numerically investigate TRSB in the model given in Eq. (1). We study the homogeneous and the inhomogeneous parts of the phase diagram separately.

A. Homogeneous phase

Consider first the mixed, homogeneous phase, i.e., the subdomain of the phase diagram where $\phi^* = 0$. Here, we can determine \mathcal{S} up to leading order in ϵ , using the standard approach of the small noise expansion [41]. Each Fourier mode is expanded as

$$\phi_{A,B}^k = \sqrt{\epsilon} \psi_{A,B}^k + \mathcal{O}(\epsilon). \quad (16)$$

Inserting this Ansatz into Eq. (1) leads to an ϵ -independent dynamical equation

$$\dot{\psi}^k(t) = \mathbb{A}_k \psi^k(t) + \xi^k, \quad (17)$$

for the leading order expansion coefficient, where

$$\mathbb{A}_k = -q_k^2 \begin{pmatrix} \alpha + \gamma q_k^2 & \kappa - \delta \\ \kappa + \delta & \beta \end{pmatrix} \quad (18)$$

is the dynamical operator obtained by linearizing Eq. (1) and $\langle \xi_A^k \xi_B^l \rangle = \langle \xi_B^k \xi_A^l \rangle = 2q_k^2/L \delta_{k,-l}$, $\langle \xi_A^k \xi_B^l \rangle = 0$. Thus, in the first-order approximation, the dynamics of the different modes in Fourier space is fully decoupled, and σ^k can be interpreted as a measure of TRSB by the k th Fourier mode. The elements of the covariance matrix of ψ^k (see Appendix D) are obtained by solving the Lyapunov equation. Noting that $\langle \phi_i^{-k} \phi_j^k \rangle = \epsilon \langle \psi_i^{-k} \psi_j^k \rangle + \mathcal{O}(\epsilon^2)$, $i, j \in \{A, B\}$ and plugging the result into Eq. (15), we obtain

$$\sigma^k = \frac{8\delta^2 q_k^2}{\alpha + \beta + \gamma q_k^2} + \mathcal{O}(\epsilon). \quad (19)$$

Equation (19) implies that it is the nonreciprocal coupling between the field components that leads to entropy production, on the scale of each Fourier mode. Specifically, each contribution depends quadratically on the degree of nonreciprocity, $\sigma^k \sim \delta^2$, which is indicative of a purely nonreciprocal origin of the entropy production [42]. Accordingly, also $\mathcal{S} \sim \delta^2$.

An important implication of Eq. (19) is the qualitatively different behavior of \mathcal{S} toward the phase boundaries to the static-demixed phase versus the dynamical phase. At the transition to the static-demixed phase, the denominator in Eq. (19) remains finite for all k , resulting in finite \mathcal{S}^* . In contrast, toward the transition to the traveling-wave phase, the denominator only remains finite for $k > 1$, but vanishes for $k = 1$. Hence, Eq. (19) implies a divergence of \mathcal{S}^* , at the transition, which can be exclusively attributed to the first Fourier mode, σ^1 . The numerical data displayed in Figs. 2(a) and 2(b) indeed supports these predictions. Equation (19) further predicts that \mathcal{S} scales like $\sim \epsilon^0$, i.e., is independent of the noise intensity at leading order, in the homogeneous phase. The comparison

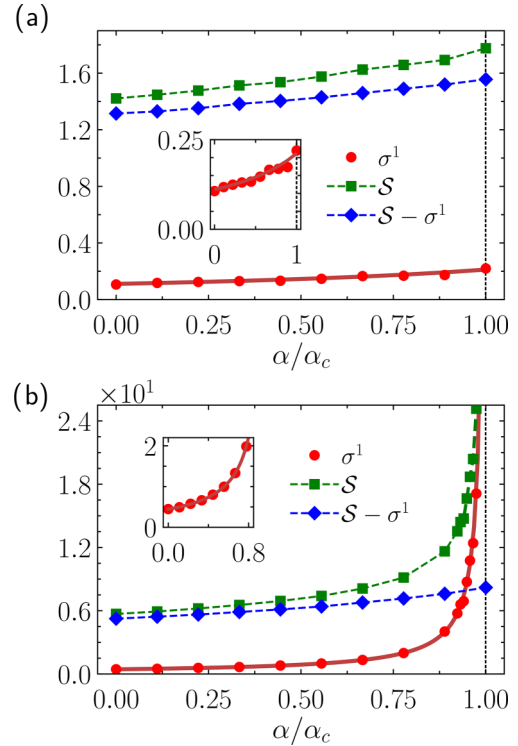


FIG. 2. Entropy production rate \mathcal{S} and the first-mode contribution σ^1 [defined in Eqs. (14), (15)] as a function of the “demixing” parameter α , inside the homogeneous phase in the vicinity of the phase boundaries (at α_c , indicated by dashed vertical lines): (a) when approaching a conventional critical point transition to the static-demixed phase along path c_1 from Fig. 1 (here, $\delta = 0.8\delta_c$); (b) approaching an oscillatory instability to the traveling-wave phase along path c_2 from Fig. 1 (here, $\delta = 1.2\delta_c$). The analytical prediction of Eq. (19) is shown by red solid lines. Symbols depict simulation results, dashed lines serve as guides to the eye. Insets depict zooms into a smaller y-axis range. We observe very distinct behavior near the transitions. Toward the static-static transition [in panel (a)], the entropy production rate only mildly increases but stays regular. Toward the static-dynamic transition [in panel (b)], the first-mode contribution σ^1 , and hence also \mathcal{S} , increase steeply, and formally diverges in the zero-noise limit, even after UV regularization. Other parameters are $\kappa = 0.01$, $\gamma = 0.015$, $\beta = 0.05$, $\epsilon = 10^{-10}$.

with the numerical data displayed in Figs. 2(a), 2(b), and 3(a) shows good agreement.

Furthermore, Eq. (19) captures another notable feature, which is confirmed by the simulation data, namely that, in the limit of small length scales, the entropy production components approach a finite positive value of

$$\lim_{k \rightarrow \infty} \sigma^k = 8\delta^2/\gamma, \quad (20)$$

which is independent of α and β . As we explicitly show in Appendix D, this does not only hold for the homogeneous phase, but Eq. (20) is in fact valid in the whole parameter range of the phase diagram, indicative of a “UV catastrophe.” The corresponding Fourier modes can be regarded as spurious degrees of freedom that could be suppressed for the present purpose, thus providing a motivation for the regularization of Eq. (14) through a UV cutoff.

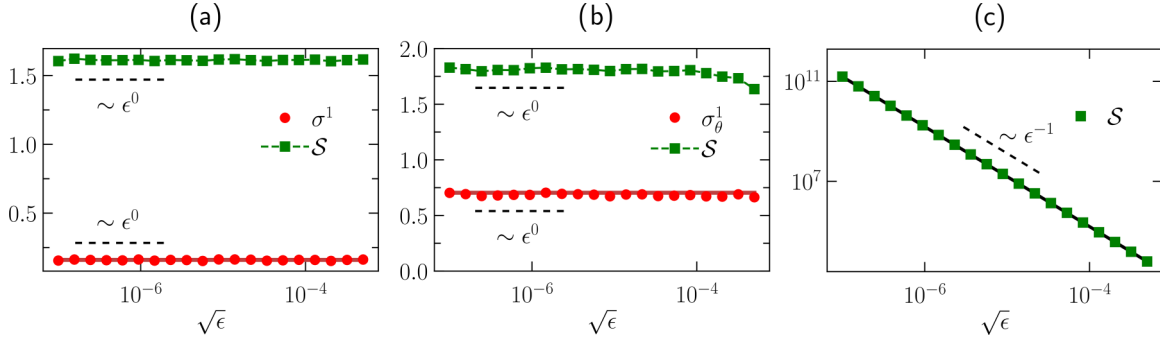


FIG. 3. Scaling of the entropy production rate \mathcal{S} and the first-mode contribution σ^1 [defined in Eqs. (14), (15), shown here in panel (a)], \mathcal{S} and σ_θ^1 [defined in Eqs. (B13) and (B8), and shown in panels (b,c)] with the noise intensity ϵ , for $\epsilon \rightarrow 0$ within the different phases: (a) Mixed phase ($\delta = 0.03$, $\alpha = -0.02$); (b) static-demixed phase ($\delta = 0.045$, $\alpha = -0.07$); (c) traveling-wave phase ($\delta = 0.06$, $\alpha = -0.07$). The analytical results for the low-noise limits given in Eqs. (19), (30), and (32) are shown by solid lines. The numerical results confirm the analytics, including that $\mathcal{S} \sim \epsilon^0$ in the static phases, and $\mathcal{S} \sim \epsilon^{-1}$ in the traveling-wave phase. Other parameters are $\kappa = 0.01$, $\gamma = 0.015$, $\beta = 0.05$.

B. Static-demixed phase

For the static-demixed phase (where $\phi^* \neq 0$), the analytical investigation turns out to be more involved than for the homogeneous phase, and requires additional steps. The first complication lies in the fact that we cannot immediately apply the small noise expansion. For a given deterministic solution ϕ^* , $\langle |\phi - \phi^*|^2 \rangle$ is of order ϵ^0 , so that we cannot directly expand $\phi - \phi^*$ in orders of $\epsilon^{1/2}$. The underlying reason is that, in the presence of noise, the position of the interfaces of the demixed state does not remain fixed, but diffuses freely. To resolve this issue, we resort to the amplitude-phase representation

$$\phi_{A,B}^k = \frac{\mathcal{A}_{A,B}^k}{2} \exp\{i\theta_{A,B}^k\} \quad (21)$$

and consider fluctuations of $\mathcal{A}_{A,B}^k$ and $\theta_{A,B}^k$, separately, within a small noise expansion. This requires the exact dynamical equations for the amplitude and the phase, for which we find

$$\begin{aligned} \dot{\mathcal{A}}_A^k &= -q_k^2 \left[(\alpha + \gamma q_k^2) \mathcal{A}_A^k + (\kappa - \delta) \mathcal{A}_B^k \cos(\theta_A^k - \theta_B^k) \right. \\ &\quad \left. + \text{Re}(\mathbf{K}^k) - \frac{4\epsilon}{L \mathcal{A}_A^k} \right] + \xi_{\mathcal{A}_A^k}, \\ \dot{\mathcal{A}}_B^k &= -q_k^2 \left[\beta \mathcal{A}_B^k + (\kappa + \delta) \mathcal{A}_A^k \cos(\theta_A^k - \theta_B^k) - \frac{4\epsilon}{L \mathcal{A}_A^k} \right] + \xi_{\mathcal{A}_B^k}, \end{aligned} \quad (22)$$

and

$$\begin{aligned} \dot{\theta}_A^k &= \frac{q_k^2}{\mathcal{A}_A^k} \left[\sin(\theta_A^k - \theta_B^k) \mathcal{A}_B^k (\kappa - \delta) - \text{Im}(\mathbf{K}^k) \right] + \xi_{\theta_A^k}, \\ \dot{\theta}_B^k &= -\frac{q_k^2}{\mathcal{A}_B^k} \sin(\theta_A^k - \theta_B^k) \mathcal{A}_A^k (\kappa + \delta) + \xi_{\theta_B^k}, \end{aligned} \quad (23)$$

with

$$\mathbf{K}^k = \sum_{l,l'} \frac{q_l^2 + 2q_l q_{l'}}{4q_k^2} \mathcal{A}_A^k \mathcal{A}_A^{l'} \mathcal{A}_A^{k-l'-l} e^{i(\theta_A^l + \theta_A^{l'} + \theta_A^{k-l'-l} - i\theta_A^k)}. \quad (24)$$

The covariance matrix of the transformed noise is still diagonal with

$$\langle \xi_{\mathcal{A}_{A,B}^k}, \xi_{\mathcal{A}'_{A,B}^l} \rangle = q_k^2 \frac{4\epsilon}{L} \delta_{kl}, \quad (25)$$

$$\langle \xi_{\theta_{A,B}^k}, \xi_{\theta'_{A,B}^l} \rangle = q_k^2 \frac{4\epsilon}{L \mathcal{A}_{A,B}^2} \delta_{kl}, \quad (26)$$

$$\langle \xi_{\mathcal{A}_A^k}, \xi_{\mathcal{A}'_B^l} \rangle = \langle \xi_{\theta_A^k}, \xi_{\theta'_B^l} \rangle = 0, \quad (27)$$

but the transformation has rendered the noise *multiplicative*. From Eqs. (22) and (23), we clearly see that unlike for $\phi^* \neq 0$, fluctuations with different wave numbers in general do not decouple. This is a general feature of any nonlinear field model.

As in Eq. (17), treating the amplitude and phase dynamics within the small noise expansion up to first order, corresponds to linearizing Eqs. (22) and (23). As we explicitly show in Appendix A, the linearized (low-noise) dynamics admits a separation into two statistically independent parts: The first part comprises all the amplitude fluctuations $\mathcal{A}_{A,B}^k$ with odd $k \in \{2n+1 : n \in \mathbb{N}_0\}$, as well as field fluctuations $\phi_{A,B}^k(t)$ of even $k \in \{2n : n \in \mathbb{N}_0\}$. This can be interpreted as the collection of fluctuations altering the amplitudes and distorting the demixing profiles of ϕ_A and ϕ_B , at a fixed position. The second part consists of the $\theta_{A,B}^k(t)$ fluctuations for odd $k \in \{2n+1 : n \in \mathbb{N}_0\}$, which may lead to displacements of the demixing profiles, as well as their dispersion. Importantly, this also includes relative translations of the profiles of fields A and B creating a characteristic phase shift $\Delta\theta^\pi = \theta_A - (\theta_B - \pi) \neq 0$, as well as joint translations. The latter can be identified as excitations of the Goldstone mode [32].

We can simplify even further by exploiting the fact that the dynamics of the model of Eq. (1) is well described by the lowest Fourier mode, alone [26]. Applying a one mode approximation in Eq. (24) corresponds to neglecting all terms that are not multiples of $(\mathcal{A}_A^1)^3$. For the phase dynamics, this yields a decoupling of θ^1 from higher Fourier modes, resulting in the approximate equation of motion

$$\dot{\theta}^1(t) = \mathbb{B}\theta^1 + \sqrt{\epsilon/L} \zeta, \quad (28)$$

with $\theta^1 = (\theta_A^1, \tilde{\theta}_B^1)^T$, $\tilde{\theta}_B^1 \equiv \theta_B^1 + \pi$,

$$\mathbb{B} = - \begin{pmatrix} (\kappa^2 - \delta^2)/\beta & -(\kappa^2 - \delta^2)/\beta \\ -\beta & \beta \end{pmatrix}, \quad (29)$$

and $\langle \zeta_i(t), \zeta_j(t') \rangle = (2/\mathcal{A}_i^{1,*})^2 \delta_{i,j} \delta(t-t')$, $i, j \in \{A, B\}$. We present in Appendix A the derivation of these closed-form expressions. In Appendix C, we provide a direct comparison between the analytical predictions by Eq. (28) and numerical results, which shows that the dynamics of the first-mode phase θ^1 is indeed accurately captured by the approximate expressions Eqs. (28) and (29) (see Fig. 6). This separation of the dynamics enables us to calculate the isolated contribution of θ^1 to the entropy production, which we denote by σ_θ^1 . It can be interpreted as measure of TRSB due to relative and joint translations of the demixing profiles. Since the emergence of the traveling wave phase can be characterized as an instability of $\theta_{A,B}^{1,*}$ [26], this contribution is of particular interest.

Interestingly, the dynamics in Eq. (28) is identical to the overdamped equations of motion of two individual degrees of freedom coupled by nonreciprocal, linear forces, each being coupled to its individual heat bath. Hence, we can draw on the results of Ref. [43], where a general expression for the entropy production of such a system is given. We find

$$\sigma_\theta^1 = 4q_1^2 \chi_B \frac{\delta^2}{\delta_c^2 - \delta^2} + \mathcal{O}(\epsilon). \quad (30)$$

This suggests that the entropy production rate scales to leading order as $\mathcal{S} \sim \epsilon^0$, just as in the homogeneous phase; implying that \mathcal{S} stays finite in the zero-noise limit. This is in line with our numerical results in Fig. 3. Furthermore, it implies that \mathcal{S} does not scale merely quadratically with the nonreciprocity, different from the homogeneous phase [see Eq. (19)]. Specifically, $\sigma_\theta^1 \sim \delta^2$ only holds for $\delta \rightarrow 0$, while it diverges like $\sigma_\theta^1 \sim (\delta_c - \delta)^{-1}$ for $\delta \rightarrow \delta_c$; indicative of the cooperative character of the emerging dynamics.

Thus, according to Eq. (30), σ_θ^1 remains regular at the static-static transition to the homogeneous phase. In contrast, concerning the transition from the static-demixed to the traveling-wave phase for $\delta \rightarrow \delta_c$, Eq. (30) predicts a surge of \mathcal{S} , driven by the phase dynamics of the first Fourier mode. These predictions are corroborated by numerical results presented in Fig. 4. As we show in Ref. [32], θ^1 can in fact further be separated into two parts; where one of them (denoted θ_c in Ref. [32]) can be identified as the dynamics along the Goldstone mode. Only this part contributes to the entropy production, such that σ_θ^1 is a direct measure of TRSB in the Goldstone mode.

Further, since the fluctuations of all the amplitudes $\mathcal{A}_{A,B}^k$, as well as the phases of $k > 1$, $\theta_{A,B}^{k>1}$, with $k \in \{2n+1 : n \in \mathbb{N}_0\}$, remain bounded toward the transition [26], we expect also the contributions to \mathcal{S} stemming from these sources to remain bounded. Indeed, our numerical results confirm that $\mathcal{S} - \sigma_\theta^1$ remains regular and rather insensitive to the transition [see Fig. 4(b)].

C. Dynamical traveling-wave phase

Last, we turn to the traveling-wave phase itself. Here, already the deterministic part of the dynamics seems to

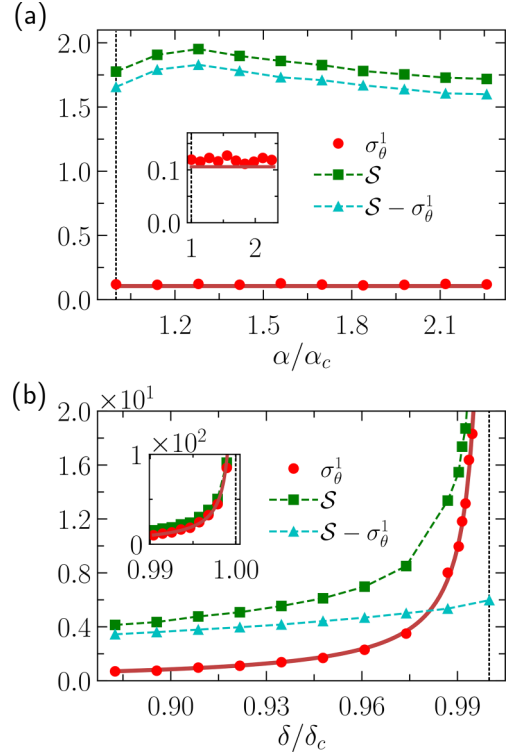


FIG. 4. Total entropy production rate \mathcal{S} from Eq. (B13), and its divergent contribution σ_θ^1 due to the first Fourier mode from Eqs. (B8), as a function of the control parameters α and δ , inside the static-demixed phase: (a) beyond the conventional critical point at α_c , along path c_3 from Fig. 1 (here, $\delta = 0.8\delta_c$), and (b) when approaching a CEP where the system undergoes a transition to the traveling-wave phase along path c_4 from Fig. 1 (here, $\alpha = -0.07$). The analytical prediction Eq. (30) is shown by red solid lines. Symbols depict simulation results, dashed lines are guides to the eye. Insets show magnifications. We observe that \mathcal{S} decreases away from the phase boundaries. For large $|\alpha|$, the data indicates saturation to a finite value. Similarly to the homogeneous phase (Fig. 2), \mathcal{S} remains regular toward to static-static transition [panel (a)], while it surges toward the static-dynamic transition [panel (b)]. The decomposition of \mathcal{S} clearly shows that the contribution σ_θ^1 from the fluctuations of the first Fourier mode, $\theta^1 = (\theta_A^1, \tilde{\theta}_B^1)^T$, is responsible for the surge in entropy production. It can exclusively be attributed to excitations of the Goldstone mode [32]. Other parameters are $\kappa = 0.01$, $\gamma = 0.015$, $\beta = 0.05$, $\epsilon = 10^{-10}$.

exhibit a broken time-reversal symmetry. Indeed, the solutions of Eq. (1) in the limit $\epsilon \rightarrow 0$ assume the form $\phi_{A,B}^*(r, t) = \varphi_{A,B}(r \pm vt)$; which clearly break the \mathcal{T} -symmetry. Thus, we expect \mathcal{S} to contain contributions from the irreversibility of the fluctuations and from the noise-independent stationary motion of the profiles. In Ref. [33] we show that the dominant contribution stemming from the deterministic motion is given by

$$\mathcal{S} = \epsilon^{-1} v^2 \int_0^L dr (|\varphi_A^*|^2 + |\varphi_B^*|^2) + \mathcal{O}(\epsilon^0). \quad (31)$$

From this expression, we can further derive an approximate solution for the leading-order contribution by the

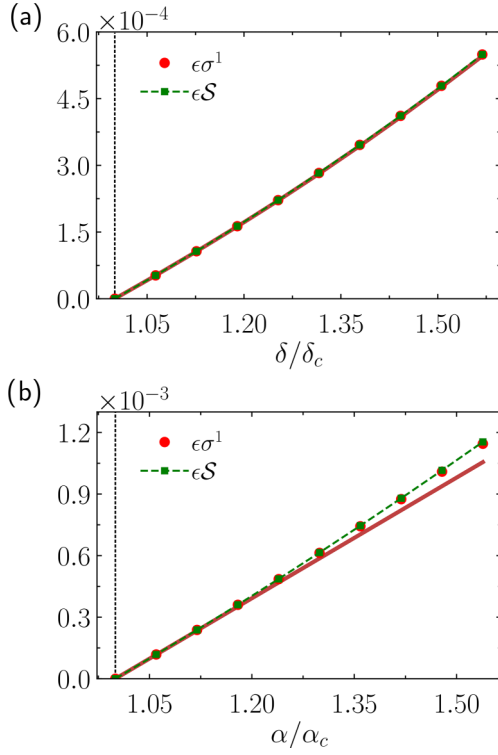


FIG. 5. Total entropy production \mathcal{S} from Eq. (B13) and its first-mode’s contribution σ^1 from Eq. (B12) within the traveling-wave phase in the vicinity of the phase boundaries: (a) beyond the CEP transition to the static-demixed phase along path c_5 from Fig. 2 (here, $\alpha = -0.07$), and (b) beyond the oscillatory instability, along path c_6 from Fig. 1 (here, $\delta = 1.2\delta_c$). The analytical result for σ^1 in Eq. (32) is shown by solid red lines, symbols depict corresponding simulation results. As one moves deeper into the traveling-wave phase, \mathcal{S} generally increases, i.e., it increases with increasing amplitude of the traveling-wave ($\mathcal{A}_{A,B}^{1,*} \propto |\alpha - \alpha_c|$ [26]), as well as with an increase of the deterministic speed of the traveling waves $v^2 \sim |\delta - \delta_c|$ [panel (a)].

first Fourier mode, as shown in Ref. [26], the solutions in the traveling-wave phase approximately take the form $\varphi_{A,B}^*(t, r) = \mathcal{A}_{A,B}^{1,*} \cos(q_1 r + vt + \theta_{A,B}^{1,*})$ with $v = \pm \sqrt{\delta^2 - \delta_c^2}$ and $\mathcal{A}_A^{1,*} = 2\sqrt{-\alpha - \gamma - \beta}$, $\mathcal{A}_B^{1,*} = \sqrt{(\delta + \kappa)/(\delta - \kappa)}\mathcal{A}_A^{1,*}$, which yields

$$\sigma^1 = \epsilon^{-1} 4L \frac{\delta(\delta^2 - \delta_c^2)}{\kappa - \delta} (\alpha + \beta + \gamma) + \mathcal{O}(\epsilon^0). \quad (32)$$

According to Eq. (32), \mathcal{S} depends *linearly* both on α and δ above the transition, in excellent agreement with the numerical data shown in Fig. 5. Equation (32) further implies that, in the low-noise regime, \mathcal{S} scales like $\sim \epsilon^{-1}$, i.e., it is dominated by the deterministic dynamics, which perfectly matches to the numerical data in Fig. 3. As a consequence, \mathcal{S}^* diverges (independently of the choice of a UV cutoff). This “physical divergence” can easily be understood from Eq. (31), which makes apparent that, in the low-noise regime, \mathcal{S} simply mirrors the presence of the deterministic “mass” current $v\varphi_{A,B}^*$.

IV. DISCUSSION

We have studied a model of two noisy Cahn-Hilliard fields with linear, asymmetric cross-coupling [26,27,34], as a prototypical example of a nonreciprocal active field theory. It admits the emergence of a dissipative order parameter pattern in the form of a traveling wave. The dynamical phase can be entered via two different static-dynamic phase transitions, an oscillatory instability or a critical exceptional point, respectively, which are both characteristic for many-body systems with nonreciprocal interactions [13].

For the three distinct phases of the model (homogeneous, static-demixed, and traveling-wave phase), we found perturbative analytical expressions for the irreversibility measure \mathcal{S} . For the homogeneous phase and for the traveling-wave phase, these become asymptotically exact in the limit of vanishing noise intensity. For the static-demixed phase, we had to refine the approach and make some additional simplification to tackle the problem analytically. The approximate results thereby obtained are indeed in excellent agreement with our numerical data, especially near the phase boundaries.

In the vicinity of the phase transitions, \mathcal{S} essentially exhibits two different types of behavior. Along the transition line connecting the two static phases of the model, we find that \mathcal{S}^* is finite and continuous, despite a diverging susceptibility, at the transition [33]. In contrast, across both static-dynamic transitions, we observe a massive increase in entropy production that already starts in the static phases. This is particularly interesting in view of the fact that the respective static phases themselves (homogeneous and static-demixed) appear, at first glance, indistinguishable from the corresponding equilibrium phases. The surge of entropy production means that the formation of the dynamical phase is heralded by a gradual, yet drastic increase of irreversible mesoscale dynamics; a feature which would be hidden when looking at the corresponding zero-temperature model. These numerical and analytical results for the nonreciprocal Cahn-Hilliard model corroborate and illustrate our general predictions for the TRSB across the continuous phase transitions of a broad class of non-Hermitian field models, presented in the two companion papers [32,33].

Additionally, our explicit perturbative calculations for the nonreciprocal Cahn-Hilliard model shed light on the origin and scale-dependence of TRSB throughout the phase diagram. Specifically, we could attribute the surge of entropy production in both static phases exclusively to the contribution of the first Fourier mode. This means that, in this model, most of the TRSB occurs through the coherently activated long-wavelength dynamics, as might have been expected for an emerging dissipative mesoscale pattern.

Our analytical considerations moreover revealed the concrete dependence of the entropy production on the strength of nonreciprocity, δ , throughout the phase diagram. This aspect deserves some further discussion. First, we found that in the homogeneous phase, $\mathcal{S} \sim \delta^2$ [see Eq. (19)]. In contrast, in the static-demixed phase, $\mathcal{S} \sim \delta^2$ holds only close to equilibrium ($\delta = 0$). Near the transition to the dynamical phase, the contribution to leading order in ϵ scales as $(\delta_c - \delta)^{-1}$ [see Eq. (30)], revealing a threshold mechanism for wave propagation. Finally, in the dynamical phase itself, close to the transition, \mathcal{S} depends linearly on $\delta - \delta_c$, to leading order

in ϵ [Eq. (32)]. Further away from the transition, $\mathcal{S} \sim \delta^2$. Thus, in the low-noise regime, the δ -dependence of \mathcal{S} is phase sensitive. Notably, this interesting δ -dependence only becomes apparent when a suitable regularization (UV cutoff) is introduced. Otherwise, the relevant properties of \mathcal{S} are obscured by trivial but overwhelming contributions of spurious (and entirely redundant) degrees of freedom [see Eq. (20) and Appendix D].

A particularly interesting insight gained from the analytical treatment concerns the TRSB in the static-demixed phase. Specifically, we could show that the main part of the entropy production stems for the fluctuations that lead to displacements of the demixing profiles (rather than their distortion). Building upon our expressions Eqs. (28) and (29), we could further formally map the interface dynamics to the dissipative ballistic motion of an *active Ornstein-Uhlenbeck particle*, providing a vivid and palpable mechanistic particle interpretation for the TRSB in the active field theory [32]. Since the active interface dynamics resides in a Goldstone mode of the model, one may say that it sacrifices its mesoscale time-translation invariance to restore the broken spatial (translational) symmetry more effectively. This ‘‘accumulation’’ of TRSB in the first Fourier mode, and its active-particle interpretation, could also be subsumed under the term ‘‘active Goldstone modes.’’

Finally, it is interesting to compare the scaling of \mathcal{S} in the noise intensity to other active field theories. Earlier works [30,31,44] have studied it in systems that display activity-driven pattern formation, such as motility-induced phase separation in active model B or B^+ [30,31], and a flocking phase in polar active models [44]. In all of these models, it was found that \mathcal{S} scales like $\sim \epsilon^1$ within the homogeneous phases, implying time-symmetric, equilibrium-like dynamics in the limit $\epsilon \rightarrow 0$. Only in the phase-separated [30,31] or polar [44] state, \mathcal{S} scales like $\sim \epsilon^0$ and hence remains finite in the zero-noise limit. In contrast, we found that, in the presence of nonreciprocal coupling, \mathcal{S} remains nonzero in the noise-free limit throughout the whole phase diagram, including the homogeneous phase, revealing that the nonreciprocal coupling is a qualitatively different (inherent) source of irreversibility.

In future studies, it could be interesting to extend the investigation of noise-induced interface motion, observed in the one-dimensional nonreciprocal Cahn-Hilliard model, to higher dimensions where more complex interface geometries could arise. Another perspective would be the extension of our considerations to more complex models, such as mesoscopic descriptions for active-passive mixtures [8], where a nonreciprocal coupling between the active and passive coarse-grained fields naturally emerges. More generally, one could explore the range of possibilities for concrete atomistic realizations that can, on the mesoscale, be subsumed into the studied nonreciprocal Cahn-Hilliard phenomenology. In particular, it could be interesting to see whether these comprise both cases in which the dynamic symmetry breaking arises on the single particle level [45] and on the many-body level [13],

respectively. Another possible direction could be to study thermodynamic embeddings, similar to the one described in Ref. [46], and to complement the model by a field that fuels the TRSB fluctuations.

We note that simultaneously and independently of ours, a recent study [47] reported consistent results concerning TRSB in the nonreciprocal Cahn-Hilliard model, but without analytically investigating the behavior of the entropy production at the transitions and in the static phases, as we present in Eqs. (19) and (30).

ACKNOWLEDGMENTS

S.L. acknowledges funding by the Deutsche Forschungsgemeinschaft (DFG) through the Walter Benjamin Stipendium (Project No. 498288081), and through the Marie-Curie fellowship (Grant No. EP/X031926/1) undertaken by the UKRI. T.S. acknowledges financial support by the pre-doc award program at Leipzig University. S.L. thanks the Physics Institutes of Leipzig University for their hospitality during several research stays.

APPENDIX A: COUPLING OF DIFFERENT FOURIER MODES IN THE DEMIXED STATE

In this Appendix, we outline our approach to tackle analytically the fluctuations in the static-demixed phase, described in Sec. III B. Specifically, we here show that the stochastic dynamics can be separated into two parts: fluctuations of the amplitude $\{\mathcal{A}^k\}$ with odd $k \in \{2n+1 : n \in \mathbb{N}_0\}$, as well as all fluctuations of $\phi_{A,B}^k$ for even k , and second, fluctuations of $\{\theta^j\}$ which encode the dispersion and displacements of the demixing profiles, see Sec. III B. Furthermore, concerning the second part, we show that within the one mode approximation, the contributing stochastic dynamics can be represented by closed-form equations for θ^1 . In the following, we will show step by step how to achieve these closed-form expressions.

First, we consider $k \in \{2n+1 : n \in \mathbb{N}_0\}$ and derive the equations of motion for \mathcal{A}^k and θ^k . To this end, we Fourier transform Eq. (1) and then apply the Itô formula to

$$\theta_{A,B}^k = \arctan \frac{\text{Im}\phi_{A,B}^k}{\text{Re}\phi_{A,B}^k}, \quad (\text{A1})$$

$$\mathcal{A}_{A,B}^k = 2\sqrt{\text{Re}\phi_{A,B}^k + \text{Im}\phi_{A,B}^k}. \quad (\text{A2})$$

Noting that the quadratic variations for the amplitude and the phase processes are determined by

$$\nabla^2 \sqrt{x^2 + y^2} = \frac{1}{\sqrt{x^2 + y^2}}, \quad (\text{A3})$$

$$\nabla^2 \arctan\left(\frac{x}{y}\right) = 0, \quad (\text{A4})$$

we thereby obtain the respective stochastic equations of motions for the amplitude and the phase dynamics, which read

$$\dot{\mathcal{A}}_A^k = -q_k^2 \left[(\alpha + \gamma q_k^2) \mathcal{A}_A^k + (\kappa - \delta) \mathcal{A}_B^k \cos(\theta_A^k - \theta_B^k) + \text{Re}(\mathbf{K}^k e^{-i\theta_A^k}) - \frac{4\epsilon}{L\mathcal{A}_A^k} \right] + \xi_{\mathcal{A}_A^k}, \quad (\text{A5})$$

$$\dot{\mathcal{A}}_B^k = -q_k^2 \left[\beta \mathcal{A}_B^k + (\kappa + \delta) \mathcal{A}_A^k \cos(\theta_A^k - \theta_B^k) - \frac{4\epsilon}{L\mathcal{A}_B^k} \right] + \xi_{\mathcal{A}_B^k}, \quad (\text{A6})$$

$$\dot{\theta}_A^k = q_k^2 \left[\sin(\theta_A^k - \theta_B^k) \frac{\mathcal{A}_B^k}{\mathcal{A}_A^k} (\kappa - \delta) - q_k^2 \text{Im}(\mathbf{K}^k e^{-i\theta_A^k}) \frac{1}{\mathcal{A}_A^k} \right] + \xi_{\theta_A^k}^k, \quad (\text{A7})$$

$$\dot{\theta}_B^k = -q_k^2 \sin(\theta_A^k - \theta_B^k) \frac{\mathcal{A}_A^k}{\mathcal{A}_B^k} (\kappa + \delta) + \xi_{\theta_B^k}^k, \quad (\text{A8})$$

with

$$\mathbf{K}^k = \sum_{l,l'} \frac{q_l^2 + 2q_l q_{l'}}{4q_k^2} \mathcal{A}_A^k \mathcal{A}_A^{l'} \mathcal{A}_A^{k-l-l'} e^{i(\theta_A^l + \theta_A^{l'} + \theta_A^{k-l-l'} - i\theta_A^k)}. \quad (\text{A9})$$

For the transformed noise terms, we find

$$\xi_{\mathcal{A}_{A,B}^k} = 4\sqrt{\frac{\epsilon}{L}} \frac{\text{Re}\phi_{A,B}^k \text{Re}\xi_{A,B}^k + \text{Im}\phi_{A,B}^k \text{Im}\xi_{A,B}^k}{\mathcal{A}_{A,B}^k}, \quad (\text{A10})$$

$$\xi_{\theta_{A,B}^k} = 4\sqrt{\frac{\epsilon}{L}} \frac{\text{Re}\phi_{A,B}^k \text{Im}\xi_{A,B}^k - \text{Im}\phi_{A,B}^k \text{Re}\xi_{A,B}^k}{(\mathcal{A}_{A,B}^k)^2}, \quad (\text{A11})$$

such that the covariance matrix again turns out to be diagonal. The transformation has rendered the noise multiplicative. The diagonal elements of its covariance matrix are given by

$$\langle \xi_{\mathcal{A}_A^k}(t) \xi_{\mathcal{A}_A^{l'}}(t') \rangle = \langle \xi_{\mathcal{A}_B^k}(t) \xi_{\mathcal{A}_B^{l'}}(t') \rangle = q_k^2 \frac{4\epsilon}{L} \delta_{kl}, \quad (\text{A12})$$

$$\langle \xi_{\theta_A^k}(t) \xi_{\theta_A^{l'}}(t') \rangle = q_k^2 \frac{4\epsilon}{L \mathcal{A}_A^2} \delta_{kl}, \quad (\text{A13})$$

$$\langle \xi_{\theta_B^k}(t) \xi_{\theta_B^{l'}}(t') \rangle = q_k^2 \frac{4\epsilon}{L \mathcal{A}_B^2} \delta_{kl}. \quad (\text{A14})$$

We parametrize the solutions of Eq. (1) for $\epsilon = 0$ as

$$\phi_{A,B}^*(r, t) = \sum_{k>0} \mathcal{A}_{A,B}^{k,*} \cos[q_k r + \theta_{A,B}^{k,*}(t)], \quad (\text{A15})$$

with wave numbers $q_k \equiv 2\pi k/L$, and odd $k \in \{2n+1 : n \in \mathbb{N}_0\}$. Since the solutions in the static-demixed state are parity symmetric [26], we can always center our r axis such that $\theta_{A,B}^{k,*} \in \{0, \pi\}$. We define

$$\begin{aligned} \Delta\theta_{A,B}^k &= \theta_{A,B}^k - \theta_{A,B}^{k,*}, \\ \Delta\mathcal{A}_{A,B}^k &= \mathcal{A}_{A,B}^k - \mathcal{A}_{A,B}^{k,*}, \end{aligned} \quad (\text{A16})$$

and therewith find that, up to linear order in $\{\Delta\theta_{A,B}^k\}$ and $\{\Delta\mathcal{A}_{A,B}^k\}$,

$$\frac{\text{Im}(\mathbf{K}^k e^{-i\theta_A^k})}{\mathcal{A}^k} = \frac{1}{4} \sum_{l,l'} (q_l^2 + 2q_l q_{l'}) \frac{\mathcal{A}_A^{l,*} \mathcal{A}_A^{l',*} \mathcal{A}_A^{k-l-l',*}}{\mathcal{A}_A^{k,*}} (\Delta\theta_A^l + \Delta\theta_A^{l'} + \Delta\theta_A^{k-l-l'} - \Delta\theta_A^k) g^{k,l,l'}, \quad (\text{A17})$$

$$\text{Re}(\mathbf{K}^k e^{-i\theta_A^k}) = \frac{1}{4} \sum_{l,l'} (q_l^2 + 2q_l q_{l'}) (\mathcal{A}_A^{l,*} \mathcal{A}_A^{l',*} \Delta\mathcal{A}_A^{k-l-l'} + \mathcal{A}_A^{l,*} \mathcal{A}_A^{1-l-l',*} \Delta\mathcal{A}_A^{l'} + \mathcal{A}_A^{l',*} \mathcal{A}_A^{1-l-l',*} \Delta\mathcal{A}_A^l) h^{k,l,l'}, \quad (\text{A18})$$

with $g^{k,l,l'} = \cos(\theta_A^{l,*} + \theta_A^{l',*} + \theta_A^{k-l-l',*} - \theta_A^{k,*})$ and

$$\sin(\theta_A^k - \theta_B^k) \frac{\mathcal{A}_B^k}{\mathcal{A}_A^k} = \cos(\theta_A^{k,*} - \theta_B^{k,*}) (\Delta\theta_A^k - \Delta\theta_B^k) \frac{\mathcal{A}_B^{k,*}}{\mathcal{A}_A^{k,*}}, \quad (\text{A19})$$

$$\sin(\theta_A^k - \theta_B^k) \frac{\mathcal{A}_A^k}{\mathcal{A}_B^k} = \cos(\theta_A^{k,*} - \theta_B^{k,*}) (\Delta\theta_A^k - \Delta\theta_B^k) \frac{\mathcal{A}_A^{k,*}}{\mathcal{A}_B^{k,*}}. \quad (\text{A20})$$

Inserting this into Eq. (A5), we see that in the regime of low-noise intensity, the dynamics of the amplitude and the phase are decoupled. Further, from $\mathcal{A}_{A,B}^{k,*} = 0$ for $k \in \{2n : n \in \mathbb{N}_0\}$,

we can conclude that all upper indices in Eqs. (A17) and (A18) are uneven. Hence, the dynamics of $\{\Delta\theta_{A,B}^k\}$ and $\{\Delta\mathcal{A}_{A,B}^k\}$ for $k \in \{2n+1 : n \in \mathbb{N}_0\}$ is decoupled from the

dynamics of ϕ^k for $k \in \{2n : n \in \mathbb{N}_0\}$. Vice versa, expanding the coupling term Eq. (A9) for even k , results only in coupling among even wave numbers. Therefore, combining all of these results, we find that the dynamics ϕ^k for $k \in \{2n+1 : n \in \mathbb{N}_0\}$ and ϕ^k for $k \in \{2n : n \in \mathbb{N}_0\}$ are mutually decoupled in the low-noise regime.

Next, for $|k| > 1$ we redefine

$$\Delta\theta_A^k \rightarrow \Delta\theta_A^k - \frac{q_k}{q_1} \Delta\theta_A^1. \quad (\text{A21})$$

Then, using $\mathcal{A}_B^{k,*}/\mathcal{A}_A^{k,*} = (\kappa + \delta)/\beta$ [26] and $\theta_A^{1,*}=0, \theta_B^{1,*}=\pi$, the equations of motion for the first Fourier mode read

$$\begin{aligned} \partial_t \Delta\theta_A^1 &= -q_k^2 (\Delta\theta_A^1 - \Delta\theta_B^1) \frac{\kappa^2 - \delta^2}{\beta} + Q + \xi_{\theta_A^1}, \\ \partial_t \Delta\theta_B^1 &= q_k^2 (\Delta\theta_A^1 - \Delta\theta_B^1) \beta + \xi_{\theta_B^1}, \end{aligned} \quad (\text{A22})$$

where the term $Q(\{\Delta\theta_A^k\}_{k>1})$, coupling different Fourier modes, is given by

$$\begin{aligned} Q(\{\Delta\theta_A^k\}_{k>1}) &= \frac{1}{4} \sum_{k,l} (q_k^2 + 2q_k q_l) \frac{\mathcal{A}_A^{k,*} \mathcal{A}_A^{l,*} \mathcal{A}_A^{1-k-l,*}}{\mathcal{A}_A^{1,*}} \\ &\times (\Delta\theta_A^k + \Delta\theta_A^l + \Delta\theta_A^{1-k-l}). \end{aligned} \quad (\text{A23})$$

Now we use that in a wide range of the phase diagram it holds that $\mathcal{A}_A^{k,*} \ll \mathcal{A}_A^{1,*}$ [26]. After careful consideration of all coefficients in Eq. (A23), we find that the most relevant one is given by $2\mathcal{A}_A^{1,*} \mathcal{A}_A^{3,*}$. Since the other coefficients in Eq. (A22) are $\mathcal{O}[(\mathcal{A}_A^{1,*})^2]$, we conclude that the term Q as a whole will have minor influence of on the dynamics of $\Delta\theta_{A,B}^1$ and can therefore approximately be neglected. This leads to a closed equation of the form of Eq. (28). Indeed, our numerical results in Appendix C show that this approximation accurately capture the properties of the exact solution.

APPENDIX B: NUMERICAL EVALUATION OF THE ENTROPY PRODUCTION RATE

Here we show how the steady-state entropy production rate \mathcal{S} can be inferred from the numerical simulation of Eq. (1). For this, we used the classical Euler-Mayurama algorithm [48]

$$s[\mathcal{A}, \theta, t, t+T] = \frac{\pi\delta}{\epsilon} \sum_k \left[\int_t^{t+T} dt \mathcal{A}_A^k \mathcal{A}_B^k (\dot{\theta}_A^k + \dot{\theta}_B^k) \sin(\theta_A^k - \theta_B^k) + \int_t^{t+T} dt (\dot{\mathcal{A}}_B^k \mathcal{A}_A^k - \dot{\mathcal{A}}_A^k \mathcal{A}_B^k) \cos(\theta_A^k - \theta_B^k) \right]. \quad (\text{B7})$$

Therefore, the contribution to \mathcal{S} associated with the dynamics of the phase can be computed by numerically evaluating the averages

$$\sigma_{\theta}^{k,\text{num}} = \pi \epsilon^{-1} \delta \mathcal{A}_A^k \mathcal{A}_B^k \left[\left\langle \frac{\theta_A^k(t+\Delta t) - \theta_A^k(t)}{\Delta t} \sin(\theta_A^k - \theta_B^k) \right\rangle + \left\langle \frac{\theta_B^k(t+\Delta t) - \theta_B^k(t)}{\Delta t} \sin(\theta_A^k - \theta_B^k) \right\rangle \right] \quad (\text{B8})$$

for each Fourier mode, resulting in the total phase contribution

$$\mathcal{S}_{\theta}^{\text{num}} = \sum_k \sigma_{\theta}^{k,\text{num}}. \quad (\text{B9})$$

Analogously, we find that the contribution to \mathcal{S} associated with the dynamics of the amplitude is given by

$$\mathcal{S}_{\mathcal{A}}^{\text{num}} = \sum_k \sigma_{\mathcal{A}}^{k,\text{num}}, \quad (\text{B10})$$

with finite difference gradients on a domain of length $L = 2\pi$, discretized by 32 equally spaced mesh points and time slices of $\Delta t = 0.01$.

For $\phi^* = 0$ the numerical entropy production rate is simply obtained by inserting the numerical results for $\text{Cov}(\phi)$ into Eq. (15). For $|\phi^*| > 0$ however, we have to apply a different approach since we want to access the contributions assigned to the amplitude and the phase dynamics, separately. This can be achieved as follows. Along the same lines as in Appendix A, we find that the equation of motion for θ^k read

$$\dot{\theta}_A^k = k^2 \sin(\theta_A^k - \theta_B^k) \frac{\mathcal{A}_B^k}{\mathcal{A}_A^k} (\kappa - \delta) + H^k + \xi_{\theta_A^k}, \quad (\text{B1})$$

$$\dot{\theta}_B^k = -k^2 \sin(\theta_A^k - \theta_B^k) \frac{\mathcal{A}_A^k}{\mathcal{A}_B^k} (\kappa + \delta) + \xi_{\theta_B^k}, \quad (\text{B2})$$

with

$$\begin{aligned} H^k &= \frac{1}{4} \sum_{l,l'} (l^2 + 2ll') \mathcal{A}_A^l \mathcal{A}_A^{l'} \mathcal{A}_A^{k-l-l'} \\ &\times \sin(\theta_A^l + \theta_A^{l'} + \theta_A^{k-l-l'} - \theta_A^k). \end{aligned} \quad (\text{B3})$$

Analogously, we find the equations of motion for the amplitude part

$$\dot{\mathcal{A}}_A^k = -k^2 \left[(\alpha + \gamma k^2) \mathcal{A}_A^k + (\kappa - \delta) \mathcal{A}_B^k - \frac{\epsilon}{\mathcal{A}_A^k} + J^k \right] + \xi_{\mathcal{A}_A^k}, \quad (\text{B4})$$

$$\dot{\mathcal{A}}_B^k = - \left[\beta \mathcal{A}_B^k + (\kappa + \delta) \mathcal{A}_A^k - \frac{\epsilon}{\mathcal{A}_B^k} \right] + \xi_{\mathcal{A}_B^k}, \quad (\text{B5})$$

with

$$\begin{aligned} J^k &= \frac{1}{4} \sum_{l,l'} (l^2 + 2ll') \mathcal{A}_A^l \mathcal{A}_A^{l'} \mathcal{A}_A^{k-l-l'} \\ &\times \cos(\theta_A^l + \theta_A^{l'} + \theta_A^{k-l-l'} - \theta_A^k). \end{aligned} \quad (\text{B6})$$

Applying the standard procedure for the computation of the entropy production rate of Langevin processes outlined in detail in Refs. [30,39], we find that the entropy production assigned to a section of the trajectory $\{\mathcal{A}(t), \theta(t)\}_{t \in [0, +\infty)}$ is given by

with

$$\sigma_{\mathcal{A}}^{k,\text{num}} = \pi \epsilon^{-1} \delta \left[\left\langle \frac{\mathcal{A}_B^k(t+t) - \mathcal{A}_B^k(t)}{\Delta t} \mathcal{A}_A^k \cos(\theta_A^k - \theta_B^k) \right\rangle - \left\langle \frac{\mathcal{A}_B^k(t+t) - \mathcal{A}_B^k(t)}{\Delta t} \mathcal{A}_A^k \cos(\theta_A^k - \theta_B^k) \right\rangle \right]. \quad (\text{B11})$$

Consequently,

$$\sigma^{k,\text{num}} = \sigma_{\mathcal{A}}^{k,\text{num}} + \sigma_{\theta}^{k,\text{num}} \quad (\text{B12})$$

and

$$\mathcal{S}^{\text{num}} = \sum_k \sigma^{k,\text{num}}. \quad (\text{B13})$$

The averages appearing in Eqs. (B8) and (B11) are directly evaluated from the simulations using at least 10^6 noise realizations. For the simulations shown in Figs. 2–5, we have chosen the numerical cutoff wave number $k = 5$ to characterize the behavior of \mathcal{S} at the transitions. We tested higher cutoffs k and obtained consistent results.

APPENDIX C: NUMERICAL VERIFICATION OF THE ONE MODE APPROXIMATION

To evaluate the validity of the closed form approximate dynamical equation for θ^1 , Eq. (28), we consider the variance of the phase fluctuations $\langle (\theta_A^1 - \theta_B^1)^2 \rangle$. We evaluate this average numerically on a domain of length $L = 2\pi$ using Eq. (28) and compare it to the analytical prediction, which is obtained as follows. Defining $\Delta\theta^\pi \equiv \theta_A^1 - \theta_B^1$ and rearranging Eq. (28), we find

$$\partial_t \Delta\theta^\pi = -\frac{(\delta_c^2 - \delta^2)}{\beta} \Delta\theta^\pi + \sqrt{\frac{2\epsilon(\Gamma_A + \Gamma_B)}{\Gamma_A \Gamma_B}} \xi_\Delta, \quad (\text{C1})$$

with

$$\Gamma_{A,B} \equiv \int_0^{2\pi} dr |\phi_{A,B}^{1,*}(r)|^2 = \pi |A_{A,B}^{1,*}|^2, \quad (\text{C2})$$

and $\langle \xi_\eta(t) \xi_\nu(t') \rangle = \delta_{\eta\nu} \delta(t - t')$. Noting that Eq. (C1) is an Ornstein-Uhlenbeck process [49], we find

$$\langle (\theta_A^1 - \theta_B^1)^2 \rangle = \epsilon \frac{\Gamma_A + \Gamma_B}{\Gamma_A \Gamma_B} \frac{\beta}{\delta_c^2 - \delta^2}, \quad (\text{C3})$$

with

$$\frac{\Gamma_A + \Gamma_B}{\Gamma_A \Gamma_B} = \frac{\beta^2 + (\delta + \kappa)^2}{4\pi(\delta + \kappa)^2 \left(\frac{\kappa^2 - \delta^2}{\beta} + \gamma - \alpha \right)}, \quad (\text{C4})$$

where we used the results [26]

$$A_A^{1,*} = 2\sqrt{\frac{\kappa^2 - \delta^2}{\beta} + \gamma - \alpha}, \quad (\text{C5})$$

$$A_B^{1,*} = \frac{\kappa + \delta}{\beta} A_A^{1,*}. \quad (\text{C6})$$

We find that the approximate analytical result Eq. (C3) is in good agreement with the numerical data [see Fig. 6], which confirms the validity of the approximation in the shown parameter regime.

APPENDIX D: STOCHASTIC DYNAMICS AND ENTROPY PRODUCTION FOR $\phi^* = 0$

Here we show how to compute \mathcal{S} in the demixed phase, i.e., for $\phi^* = 0$ up to leading order in ϵ using Eq. (15). As described in Sec. III A, the contribution from each Fourier mode ϕ^j can be obtained by computing the covariance matrix of the leading order expansion coefficient of the small noise expansion of ψ^j , which is defined as

$$\text{Cov}(\psi)_{ij}^k \equiv \langle (\psi_i^k \psi_j^{-k} - \langle \psi_i^k \rangle \langle \psi_j^{-k} \rangle)^2 \rangle. \quad (\text{D1})$$

The expansion coefficients each satisfy an ϵ -independent dynamical equation given by

$$\dot{\psi}^k(t) = \mathbb{A}_k \psi^k(t) + \xi^k, \quad (\text{D2})$$

with

$$\mathbb{A}_k = -q_k^2 \begin{pmatrix} \alpha + \gamma q_k^2 & \kappa - \delta \\ \kappa + \delta & \beta \end{pmatrix} \quad (\text{D3})$$

and

$$\langle \xi^k \xi^l \rangle = 2\epsilon \frac{q_l^2}{L} \delta_{k,-l}. \quad (\text{D4})$$

Since ϕ^* is a linearly stable fixed point, \mathbb{A}^k has full rank for each k . Hence, taking the average of Eq. (D2) we find $\langle \psi_i^k \rangle = 0$ for $i \in \{A, B\}$. Now applying the Itô formula to $\psi_i^k \psi_j^{-k}$ and averaging, we obtain the so-called Lyapunov equation assigned to Eq. (D2) which reads

$$(\text{Cov}(\psi)^{-k} (\bar{\mathbb{A}}_k)^T)_{ij} + (\mathbb{A}_k \text{Cov}(\psi)^k)_{ij} = 2\frac{\epsilon}{L} \delta_{ij}. \quad (\text{D5})$$

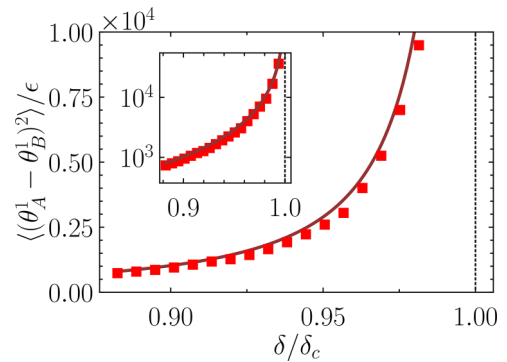


FIG. 6. Scaled variance of the phase fluctuations near the transition as a function of δ for $\alpha = -0.07$, $\beta = 0.05$, $\gamma = 0.015$, $\kappa = 0.01$, $\epsilon = 10^{-10}$ from the numerical simulation of Eq. (1). The solid line shows the analytical result Eq. (C3) which holds within the one mode approximation. The inset shows the same results in a log-scale.

The solutions for the relevant entries read

$$\begin{aligned} \langle \text{Re} \psi_A^k \psi_B^{-k} \rangle &= \frac{1}{2} (\text{Cov}(\psi)_{AB}^k + \text{Cov}(\psi)_{AB}^{-k}) \\ &= -\frac{\kappa(\alpha + \gamma q_k^2 + \beta) + \delta[\beta - (\alpha + \gamma q_k^2)]}{[(\alpha + \gamma q_k^2) + \beta][\delta^2 - \kappa^2 + (\alpha + \gamma q_k^2)\beta]} \frac{\epsilon}{L}, \end{aligned} \quad (\text{D6})$$

$$\begin{aligned} \langle |\psi_A^k|^2 \rangle &= \text{Cov}(\psi)_{AA}^k = \frac{\delta - \kappa}{(\alpha + \gamma q_k^2)} \langle \text{Re} \psi_A^k \phi_B^{-k} \rangle \\ &\quad + \frac{1}{(\alpha + \gamma q_k^2)} \frac{\epsilon}{L}, \end{aligned} \quad (\text{D7})$$

$$\langle |\phi_B^k|^2 \rangle = \text{Cov}(\psi)_{BB}^k = -\frac{\delta + \kappa}{\beta} \langle \text{Re} \psi_A^k \psi_B^{-k} \rangle + \frac{1}{\beta} \frac{\epsilon}{L}. \quad (\text{D8})$$

Noting that $\langle \phi_i^{-k} \phi_j^k \rangle = \epsilon \langle \psi_i^{-k} \psi_j^k \rangle + \mathcal{O}(\epsilon^2)$, $i, j \in \{A, B\}$ and plugging the result into Eq. (15), we obtain

$$\sigma^k = \frac{8\delta^2 q_k^2}{\alpha + \beta + \gamma q_k^2} + \mathcal{O}(\epsilon). \quad (\text{D9})$$

We note that

$$\mathbb{A}_k \sim \begin{pmatrix} \gamma q_k^2 & \kappa - \delta \\ \kappa + \delta & \beta \end{pmatrix}, \quad \text{as } k \rightarrow \infty, \quad (\text{D10})$$

which means that fluctuations become effectively decoupled for large wave numbers. Consequently, their statistics becomes independent of α and of the underlying zero-noise solution ϕ^* . Repeating the above calculation, we find

$$\langle \text{Re} \phi_A^k \phi_B^{-k} \rangle \sim \frac{1}{\gamma q_k^2} \frac{\delta - \kappa}{\beta} \frac{\epsilon}{L}, \quad (\text{D11})$$

$$\langle |\phi_A^k|^2 \rangle \sim \frac{1}{\gamma q_k^2} \frac{\epsilon}{L}, \quad (\text{D12})$$

$$\langle |\phi_B^k|^2 \rangle \sim \frac{1}{\beta} \frac{\epsilon}{L}, \quad (\text{D13})$$

as $k \rightarrow \infty$, and consequently

$$\sigma^k \sim \frac{8\delta^2}{\gamma} + \mathcal{O}(\epsilon), \quad \text{as } k \rightarrow \infty \quad (\text{D14})$$

in the whole parameter range of the phase diagram [as given in Eq. (20)]. Thus, there are always infinitely many, identical, noise-independent contributions with $\sim \delta^2$ in all phases. Physically, however, they have little significance because they come from length scales at which hydrodynamic theory loses its validity, motivating a UV cutoff.

APPENDIX E: UV CUTOFF

Since throughout the phase diagram $\sigma^k \sim \delta^2/\gamma$ as $k \rightarrow \infty$ (see Appendix D), \mathcal{S} given in Eq. (14) as a sum over infinitely many such Fourier mode contributions, formally takes the value infinity and is thus not well-defined measure of TRSB. A way of regularizing \mathcal{S} is by truncating the sum in Eq. (14) at a finite wave number k_{\max} ,

$$\mathcal{S} = \sum_{k=1}^{k_{\max}} \sigma^k. \quad (\text{E1})$$

Importantly, this method of regularizing does not spoil the genuinely probabilistic interpretation of \mathcal{S} in terms of path probabilities.

To show this, we first note that Eq. (D10) implies that above a sufficiently large wave number k_{\max} , the dynamics of each Fourier mode ϕ^k evolves independently of that of all other Fourier modes. Hence, the path probability decomposes approximately into the following product:

$$\begin{aligned} &\mathbb{P}[\{\{\phi^k\}_{t \in [0, T]}\}_{k > 0}] \\ &\approx \mathbb{P}[\{\{\phi^k\}_{t \in [0, T]}\}_{k_{\max} \geq k > 0}] \prod_{k > k_{\max}} \mathbb{P}[\{\{\phi^k\}_{t \in [0, T]}\}]. \end{aligned} \quad (\text{E2})$$

Consequently, the series representation of \mathcal{S} in Eq. (E1) can be approximately decomposed as

$$\mathcal{S} \approx \mathcal{S}[\{\{\phi^k\}_{t \in [0, T]}\}_{k_{\max} \geq k > 0}] + \sum_{k > k_{\max}} \mathcal{S}[\{\{\phi^k\}_{t \in [0, T]}\}], \quad (\text{E3})$$

with

$$\mathcal{S}[\{\{\phi^k\}_{t \in [0, T]}\}_{k_{\max} \geq k > 0}] \approx \sum_{k=1}^{k_{\max}} \sigma^k \quad (\text{E4})$$

and

$$\mathcal{S}[\{\{\phi^k\}_{t \in [0, T]}\}] \approx \sigma^k \quad \text{for } k > k_{\max}. \quad (\text{E5})$$

This allows us to conclude that \mathcal{S} in Eq. (E1) can be understood as the sum of the entropy productions of an infinite number of individual processes, each of which is finite and is therefore naturally divergent.

Since the spurious high Fourier modes with $\sigma^k \sim \delta^2/\gamma$ as $k \rightarrow \infty$, represent physically irrelevant or even unphysical degrees of freedom that all produce entropy, it is actually rather the regularized, truncated series which should be understood as a realistic measure of TRSB (in the sense of a path probability ratio) of the physically pertinent mesoscale dynamics.

- [1] P. J. Wangersky, Lotka-Volterra population models, *Annu. Rev. Ecol. Evol. Syst.* **9**, 189 (1978).
- [2] L. Barberis and F. Peruani, Large-scale patterns in a minimal cognitive flocking model: Incidental leaders, nematic patterns, and aggregates, *Phys. Rev. Lett.* **117**, 248001 (2016).
- [3] S. A. M. Loos, S. H. L. Klapp, and T. Martynec, Long-range order and directional defect propagation in the nonreciprocal XY model with vision cone interactions, *Phys. Rev. Lett.* **130**, 198301 (2023).
- [4] L. P. Dadhichi, J. Kethapelli, R. Chajwa, S. Ramaswamy, and A. Maitra, Nonmutual torques and the unimportance of motility

for long-range order in two-dimensional flocks, *Phys. Rev. E* **101**, 052601 (2020).

- [5] K. Hayashi and S. I. Sasa, The law of action and reaction for the effective force in a non-equilibrium colloidal system, *J. Phys.: Condens. Matter* **18**, 2825 (2006).
- [6] B. Liebchen and A. K. Mukhopadhyay, Interactions in active colloids, *J. Phys.: Condens. Matter* **34**, 083002 (2022).
- [7] F. A. Lavergne, H. Wendehenne, T. Bäuerle, and C. Bechinger, Group formation and cohesion of active particles with visual perception-dependent motility, *Science* **364**, 70 (2019).

- [8] R. Wittkowski, J. Stenhammar, and M. E. Cates, Nonequilibrium dynamics of mixtures of active and passive colloidal particles, *New J. Phys.* **19**, 105003 (2017).
- [9] M. Agrawal, I. R. Bruss, and S. C. Glotzer, Tunable emergent structures and traveling waves in mixtures of passive and contact-triggered-active particles, *Soft Matter* **13**, 6332 (2017).
- [10] R. Mandal, S. S. Jaramillo, and P. Sollich, Robustness of travelling states in generic non-reciprocal mixtures, [arXiv:2212.05618](https://arxiv.org/abs/2212.05618).
- [11] A. M. Menzel and H. Löwen, Traveling and resting crystals in active systems, *Phys. Rev. Lett.* **110**, 055702 (2013).
- [12] S. Ghosh, S. Gutti, and D. Chaudhuri, Pattern formation, localized and running pulsation on active spherical membranes, *Soft Matter* **17**, 10614 (2021).
- [13] M. Fruchart, R. Hanai, P. B. Littlewood, and V. Vitelli, Non-reciprocal phase transitions, *Nature (London)* **592**, 363 (2021).
- [14] L. Demarchi, A. Goychuk, I. Maryshev, and E. Frey, Enzyme-enriched condensates show self-propulsion, positioning, and coexistence, *Phys. Rev. Lett.* **130**, 128401 (2023).
- [15] M. Knežević, T. Welker, and H. Stark, Collective motion of active particles exhibiting non-reciprocal orientational interactions, *Sci. Rep.* **12**, 19437 (2022).
- [16] E. Sesé -Sansa, D. Levis, and I. Pagonabarraga, Microscopic field theory for structure formation in systems of self-propelled particles with generic torques, *J. Chem. Phys.* **157**, 224905 (2022).
- [17] L. Braverman, C. Scheibner, B. VanSaders, and V. Vitelli, Topological defects in solids with odd elasticity, *Phys. Rev. Lett.* **127**, 268001 (2021).
- [18] A. Poncet and D. Bartolo, When soft crystals defy Newton's third law: Nonreciprocal mechanics and dislocation motility, *Phys. Rev. Lett.* **128**, 048002 (2022).
- [19] M. C. Cross and P. C. Hohenberg, Pattern formation outside of equilibrium, *Rev. Mod. Phys.* **65**, 851 (1993).
- [20] M. Cross and H. Greenside, *Oscillatory patterns*, in *Pattern Formation and Dynamics in Nonequilibrium Systems* (Cambridge University Press, Cambridge, UK, 2009), pp. 358–400.
- [21] R. El-Ganainy, K. G. Makris, M. Khajavikhan, Z. H. Musslimani, S. Rotter, and D. N. Christodoulides, Non-Hermitian physics and PT symmetry, *Nat. Phys.* **14**, 11 (2018).
- [22] A. Krasnok, N. Nefedkin, and A. Alu, Parity-time symmetry and exceptional points: A tutorial, [arXiv:2103.08135](https://arxiv.org/abs/2103.08135).
- [23] R. Hanai and P. B. Littlewood, Critical fluctuations at a many-body exceptional point, *Phys. Rev. Res.* **2**, 033018 (2020).
- [24] P. Hohenberg and A. Krekhov, An introduction to the Ginzburg–Landau theory of phase transitions and nonequilibrium patterns, *Phys. Rep.* **572**, 1 (2015).
- [25] I. Bose and S. Ghosh, Bifurcation and criticality, *J. Stat. Mech.* (2019) 043403.
- [26] Z. You, A. Baskaran, and M. C. Marchetti, Nonreciprocity as a generic route to traveling states, *Proc. Natl. Acad. Sci. USA* **117**, 19767 (2020).
- [27] S. Saha, J. Agudo-Canalejo, and R. Golestanian, Scalar active mixtures: The nonreciprocal Cahn–Hilliard model, *Phys. Rev. X* **10**, 041009 (2020).
- [28] T. Frohoff-Hülsmann and U. Thiele, Nonreciprocal Cahn–Hilliard model emerges as a universal amplitude equation, *Phys. Rev. Lett.* **131**, 107201 (2023).
- [29] R. Hanai, Non-reciprocal frustration: Time crystalline order-by-disorder phenomenon and a spin-glass-like state, [arXiv:2208.08577](https://arxiv.org/abs/2208.08577).
- [30] Y. I. Li and M. E. Cates, Steady state entropy production rate for scalar Langevin field theories, *J. Stat. Mech.* (2021) 013211.
- [31] C. Nardini, É. Fodor, E. Tjhung, F. van Wijland, J. Tailleur, and M. E. Cates, Entropy production in field theories without time-reversal symmetry: Quantifying the non-equilibrium character of active matter, *Phys. Rev. X* **7**, 021007 (2017).
- [32] T. Suchanek, K. Kroy, and S. A. M. Loos, companion paper, Irreversible mesoscale fluctuations herald the emergence of dynamical phases, *Phys. Rev. Lett.* **131**, 258302 (2023).
- [33] T. Suchanek, K. Kroy, and S. A. M. Loos, companion paper, Time-reversal and parity-time symmetry breaking in non-Hermitian field theories, *Phys. Rev. E* **108**, 064123 (2023).
- [34] T. Frohoff-Hülsmann, J. Wrembel, and U. Thiele, Suppression of coarsening and emergence of oscillatory behavior in a Cahn–Hilliard model with nonvariational coupling, *Phys. Rev. E* **103**, 042602 (2021).
- [35] R. Kubo, The fluctuation-dissipation theorem, *Rep. Prog. Phys.* **29**, 255 (1966).
- [36] T. Frohoff-Hülsmann, U. Thiele, and L. M. Pismen, Non-reciprocity induces resonances in a two-field Cahn–Hilliard model, *Philos. Trans. R. Soc. A* **381**, 20220087 (2023).
- [37] Y. Ashida, Z. Gong, and M. Ueda, Non-Hermitian physics, *Adv. Phys.* **69**, 249 (2020).
- [38] J. O’Byrne, Nonequilibrium currents in stochastic field theories: A geometric insight, *Phys. Rev. E* **107**, 054105 (2023).
- [39] U. Seifert, Entropy production along a stochastic trajectory and an integral fluctuation theorem, *Phys. Rev. Lett.* **95**, 040602 (2005).
- [40] To be well-defined, the ratio of path probabilities in Eq. (7) is to be interpreted in terms of the Onsager–Machlup formalism [50].
- [41] C. Gardiner, *Stochastic Methods* (Springer, Berlin, 2009), Vol. 4.
- [42] Indeed, the sole presence of a nonreciprocal coupling in a system of two overdamped or underdamped particles would also yield an entropy production rate $\sim \delta^2$ [43].
- [43] S. A. M. Loos and S. H. L. Klapp, Irreversibility, heat and information flows induced by non-reciprocal interactions, *New J. Phys.* **22**, 123051 (2020).
- [44] Ø. Borthne, É. Fodor, and M. Cates, Time-reversal symmetry violations and entropy production in field theories of polar active matter, *New J. Phys.* **22**, 123012 (2020).
- [45] X. Wang, P.-C. Chen, K. Kroy, V. Holubec, and F. Cichos, Spontaneous vortex formation by microswimmers with retarded attractions, *Nat. Commun.* **14**, 56 (2023).
- [46] T. Markovich, É. Fodor, E. Tjhung, and M. E. Cates, Thermodynamics of active field theories: Energetic cost of coupling to reservoirs, *Phys. Rev. X* **11**, 021057 (2021).
- [47] H. Alston, L. Cocconi, and T. Bertrand, companion paper, Irreversibility across a nonreciprocal \mathcal{PT} -symmetry-breaking phase transition, *Phys. Rev. Lett.* **131**, 258301 (2023).
- [48] E. Platen and N. Bruti-Liberati, *Numerical Solution of Stochastic Differential Equations with Jumps in Finance* (Springer Science & Business Media, Berlin, 2010), Vol. 64.
- [49] G. E. Uhlenbeck and L. S. Ornstein, On the theory of the Brownian motion, *Phys. Rev.* **36**, 823 (1930).
- [50] L. Onsager and S. Machlup, Fluctuations and irreversible processes, *Phys. Rev.* **91**, 1505 (1953).